2026 IEEE International Conference on Robotics and Automation (ICRA 2026)
June 1-5, 2026. Vienna, Austria

Implicit LiDAR SLAM with Confidence-Guided SDF and Normal-Driven Sampling

Hong Liu[1]*, Feixuan Huang[1]*, Wang Gao[1], Jinle Xu[1], Shuguo Pan[1], and Keck-Voon Ling[2]

***Abstract*—Implicit representations for LiDAR-based Simultaneous Localization and Mapping (SLAM) offer significant advantages in storage efficiency and expressive power over traditional explicit maps. However, a critical limitation for implicit SLAM is their deterministic nature, which prevents the quantification of prediction uncertainty in sparse or noisy conditions. Furthermore, the accuracy of the underlying Signed Distance Field (SDF) is often compromised by systematic errors arising from the angular dependency of LiDAR measurements, where oblique incident angles lead to biased distance estimations and degrade map quality. To address these challenges, this paper introduces a framework that enhances the robustness and accuracy of implicit LiDAR SLAM by integrating uncertainty estimation and an adaptive sampling strategy. We propose a neural network-based approach to learn and predict SDF uncertainty, which is then effectively incorporated into both localization and mapping processes. Concurrently, to mitigate incident angle-induced errors, we develop an adaptive sampling scheme that weights LiDAR rays based on surface normal information. Validation on public datasets and a custom experimental platform demonstrates that our approach outperforms baseline methods in terms of localization, mapping accuracy, and robustness.**

***Index Terms*—LiDAR, SLAM, Signed Distance Field, Uncertainty**

I. INTRODUCTION

Light Detection and Ranging (LiDAR) map representations can be categorized into explicit and implicit approaches. Explicit maps utilize voxels, meshes, or other geometric primitives to directly reconstruct the surrounding environment [1] [2]. While most explicit representations maintain the completeness and fidelity of raw sensor data, they suffer from substantial storage overhead and require effective downsampling and map management strategies for large-scale environmental deployment. In contrast, implicit maps [3] [4] encode the environmental structure through functional mappings rather than direct storage of geometric information, offering advantages in storage efficiency and representational expressiveness.

Implicit LiDAR Simultaneous Localization and Mapping (SLAM) systems can serve as the foundation for perception and planning modules [5]. Current applications of LiDAR in implicit representations are primarily driven by Signed Distance Field (SDF), which capture the signed distance to the nearest surface through continuous functions [6]. Although implicit mapping has shown success in scene reconstruction and novel view synthesis [7], existing models are generally deterministic and lack a probabilistic framework to quantify prediction confidence. This limitation becomes critically important in real-world deployment scenarios involving sparse or noisy sensor data and occluded environments, where unreliable predictions may result in system failures. In the field of visual Neural Radiance Field (NeRF), approaches include Bayesian-based methods and learning-based methods to improve uncertainty quantification [8] [9]. Nevertheless, these techniques are primarily tailored for indoor small-scale scenes and present limitations when deployed in outdoor large-scale environments. In our work, we adopt a learning-based approach while maintaining the real-time performance requirements of implicit LiDAR SLAM systems.

Furthermore, the implicit mapping training faces inherent challenges due to the angular dependency of LiDAR measurements. The incident angle between LiDAR rays and object surfaces introduces systematic errors that compromise the accuracy of SDF value estimation. When laser beams strike surfaces at oblique angles, the measured distances deviate from the true perpendicular distances to the surface, resulting in biased SDF values that can degrade mapping quality. While existing research [10] [11] has attempted to correct SDF values by compensating for incident angle effects, establishing accurate mathematical models to obtain precise corrected values remains challenging. The combined effects of surface geometry, material properties, beam divergence, and incidence angles [12] make closed-form corrections challenging, while empirical approximations lack robustness.

To tackle these issues, the main contributions of this work are as follows:

- We propose a neural network-based approach to learn and estimate SDF uncertainty in implicit SLAM, and effectively incorporate this uncertainty into subsequent localization and mapping processes.
- We develop an adaptive sampling scheme that computes LiDAR ray weights according to surface normal information derived from point cloud data.
- We validate the effectiveness of our proposed method for localization and mapping on both public datasets and a custom experimental platform, demonstrating improve-

---

This work was supported by Science and Technology Major Project of Jiangsu Province (Grant No.BG2024003). Corresponding author: Wang Gao (E-mail: gaow@seu.edu.cn).

[1]Hong Liu, Feixuan Huang, Wang Gao, Jinle Xu, and Shuguo Pan are with School of Instrument Science and Engineering, State Key Laboratory of comprehensive PNT Network and Equipment Technology, Southeast University, Nanjing 210096, China.

[2]Keck-Voon Ling is with the School of Electrical and Electronic Engineering, Nanyang Technological University, Singapore 639798.

* denotes that Hong Liu and Feixuan Huang contribute equally to this work.

ments in both accuracy and robustness.

II. RELATED WORK

A. Implicit Representation Methods

Implicit maps represent environments through continuous functions, mainly realized using neural networks and spherical harmonics.

Neural implicit representations have advanced rapidly in recent years. NICE-SLAM [13] introduces implicit neural representations into visual SLAM, employing multilayer perceptrons (MLP) to encode geometric and appearance information of the scene. Shine-Mapping [3] specifically designs an incremental neural implicit mapping framework for LiDAR data, leveraging hierarchical feature grids to accelerate training and querying. Recent advances in implicit SLAM have demonstrated the effectiveness of leveraging implicit map representations for frame-to-map registration. Notable examples include [14] and [15], which achieve simultaneous localization and implicit map construction.

Spherical harmonic representations [16] exploit the orthogonality of spherical basis functions to encode environmental information into frequency-domain coefficients. This method is particularly effective for representing continuous fields such as illumination and reflectance. CURL-SLAM [17] converts point clouds into spherical harmonic representations to achieve a lightweight map representation; however, this approach does not yet offer competitive advantages in localization accuracy.

B. Confidence Evaluation in LiDAR SLAM

Explicit SLAM methods improve localization precision by leveraging geometric primitives to identify and mitigate outlier influences [18]. The confidence assessment in these approaches is carried out through geometric analysis, which includes examining point-cloud structures and evaluating optimization characteristics such as eigenvalues [19], the condition number [20] and the Fisher information matrix [21]. In parallel, data-driven methodologies have gained prominence as viable uncertainty quantification alternatives, facilitated by advances in machine learning paradigms [22] [23]. These techniques leverage large-scale real-world datasets and learned representations to model uncertainty distribution, however, they require substantial amounts of ground-truth data for supervision.

In implicit representations, UN3-Mapping [24] introduce the gradient fields and quantifies uncertainty through heteroscedastic models to improve mapping quality. However, it lacks a localization module and is not a complete SLAM system. Uni-SLAM [25] proposes a predictive uncertainty method for image depth that weights the loss function accordingly. Gui et al. [26] introduce maximum probability density function constraints to determine SDF confidence levels. Compared to these existing methods, our work introduces uncertainty modeling into the real-time LiDAR SLAM, leveraging uncertainty information to improve both localization and mapping quality.

C. Normal Vector in LiDAR SLAM

LOG-LIO [27] proposes a computationally efficient normal vector estimation algorithm and leverages the extracted local geometric information to prioritize point-to-surfel matching during scan registration, significantly reducing computational overhead while maintaining mapping accuracy. Building upon geometric feature extraction, Chung et al. [28] leverage normal vectors extracted from LiDAR point cloud for multiple critical tasks including point cloud matching, degeneracy detection, and loop closure detection, thereby ensuring robust and reliable SLAM performance particularly in geometrically constrained narrow indoor environments where traditional feature-based methods may fail. Similarly, II-NVM [29] incorporates normal vector consistency constraints to enhance mapping accuracy, with particular focus on addressing indoor environmental challenges.

In the implicit mapping module, Song et al. [11] utilizes normal vectors to compute more accurate SDF values. While their approach focuses on improving SDF accuracy, our method extends the utilization of normal vectors by computing incident angles to determine adaptive sampling weights.

III. METHODOLOGY

A. System Overview

Fig. 1 shows the system framework. The system adopts the neural point organization method described in [15]. Following motion compensation of each point cloud frame, we extract local map within the vicinity of the current position. These sampled points are subsequently queried via a neural network to retrieve the corresponding SDF and uncertainty values, which are then fed into an implicit matching module to perform registration and determine the optimal pose estimation. In the preprocessing stage for training, normal vectors are computed for the point cloud samples. These normal vectors facilitate the calculation of incidence angles, from which sampling weights are derived. The binary cross-entropy loss function, uncertainty loss, and regularization loss guide the optimization process to obtain optimal parameters for the neural point representation.

B. Normal Vector-Based Sampling Strategy

Fig. 2 illustrates the schematic diagram of LiDAR beam reflection on object surfaces. When the laser beam is incident perpendicularly on the target surface (i.e., $\theta = 0$), the reflected signal exhibits the maximum intensity, resulting in the highest ranging accuracy. Consequently, these measurements are assigned higher confidence weights. In contrast, at larger incidence angles (approaching grazing incidence), the effects of surface scattering, reduced reflected energy, and geometric distortions significantly increase measurement errors, necessitating a reduction in their weight contributions. To address this challenge, we introduce a cosine-based weighting approach that leverages normal vectors to automatically recognize and quantify the reliability of measurements under varying incidence conditions.

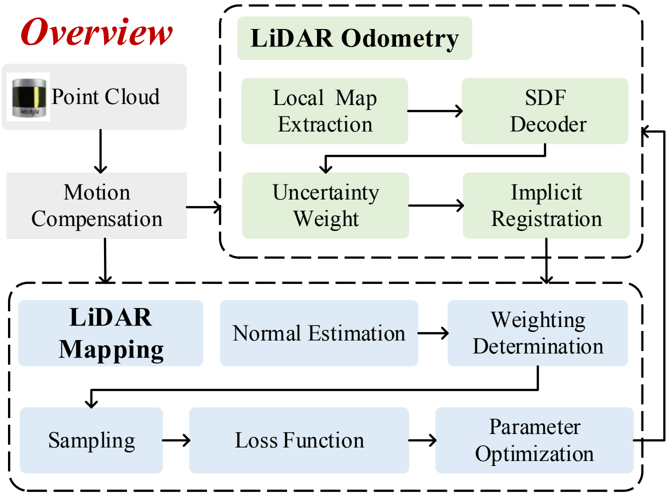

Fig. 1: System framework overview showing the integration of normal vector-based sampling with uncertainty quantification.

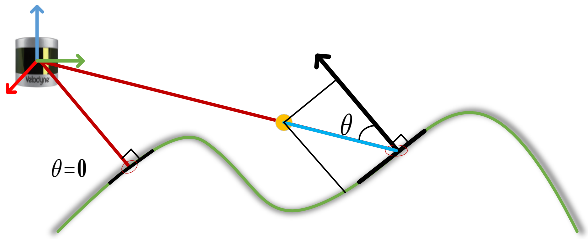

Fig. 2: The yellow dots represent sampling points. The red lines indicate incident rays, while the blue lines show that the SDF values in this segment correspond to oblique incidence, which deviates from the true SDF values.

The normalized ray direction vector is defined as $\hat{\mathbf{r}} = \frac{\mathbf{p}_e}{||\mathbf{p}_e||}$, where $\mathbf{p}_e$ is the coordinate of the end point. For the i-th sampling point $\mathbf{p}_i$, it is defined as $\mathbf{p}_i = c\hat{\mathbf{r}}$, where c is the length along the ray. Surface normal vectors are first computed for each point using the Open3D library's normal estimation algorithms, which employ k-nearest neighbor search and principal component analysis to determine local surface orientations. The estimated normal vectors are normalized to obtain unit vectors $\hat{\mathbf{n}}$. Subsequently, the cosine of the angle between the ray direction and surface normal can be computed as

$$\cos\theta = \hat{\mathbf{r}} \cdot \hat{\mathbf{n}} \tag{1}$$

The incidence angle-based weight factor $w_{\text{inc},i}$ about sampling point $\mathbf{p}_i$ can be defined as

$$w_{\text{inc},i} = |\cos\theta_i|^{\alpha} \tag{2}$$

where α is the angle of incidence exponent parameter that controls the weight decay strength. The validation process for the selection of this parameter value is presented in Section IV-E.

For comprehensive scene geometry capture, the sample points distribution $\mathcal{N}$ is learned through samples distributed using a Gaussian probability model centered at distance l with variance ${\beta_s}^2$, where l represents the mean of all sampling distances along the ray. The distance for surface sampling points l_s can be formulated as

$$l_s \sim \mathcal{N}\left(l, \beta_s^2\right) \tag{3}$$

To enable accurate reconstruction of fine-scale objects while creating spatial carving effects, the sampling strategy incorporates uniform distribution U of points throughout the free space region preceding the surface, with $\zeta_{\min}$ establishing the minimum sampling depth ratio. Front-surface sampling distances l_f can be represented as:

$$l_f \sim U\left(\zeta_{\min} l, l - 2\beta_s\right) \tag{4}$$

Additionally, sampling is also performed behind the surface as

$$l_h \sim U\left(l + 2\beta_s, l + l_{max}\right) \tag{5}$$

where l_h is the behind-surface sampling distance and l_{max} defines the maximum sampling distance. Taking into account all sampling points, where $\mathbf{p}_i$ represents one of these sampling points, we need to compute its weight during the training process. In [15], authors use the reciprocal of the standard deviation β as weights, denoted as W_i. In contrast to this approach, we further consider the weighted influence of incidence angles computed from normal vectors, and the modified formula is

$$W_i^{\text{final}} = W_i \times w_{\text{inc},i} \tag{6}$$

where W_i^{final} is the final weight. This method is simple and effective. Compared to other approaches that incorporate normal vector information into the training process [11] [24], it avoids increasing the training computational burden through additional constraints while maintaining competitive mapping performance.

C. Confidence-Guided Model

A conceptual illustration of SDF measurement residuals is presented in Fig. 3. The diagram depicts the deviation between true SDF isolines (green solid curves) and measured SDF isolines (red dashed curves) around an object boundary. ε indicate the measurement residuals. As supervisory signals, they are also subject to computational inaccuracies, therefore the uncertainty of SDF values must be taken into consideration. Our approach employs a probabilistic framework to simultaneously predict SDF values and their associated epistemic uncertainties. We assume the predicted SDF and uncertainty values corresponding to input feature x_i follow a Gaussian distribution $\mathcal{G}$, which is given by

$$\hat{s}_i \sim \mathcal{G}\left(f_\theta\left(x_i\right), \sigma_\theta^2\left(x_i\right)\right) \tag{7}$$

where $\hat{s}_i$ is the SDF value predicted by the MLP, $f_\theta\left(x_i\right)$ represents the mean, and $\sigma_\theta^2\left(x_i\right)$ denotes the learned variance function. To ensure variance estimates while maintaining numerical stability, we employ a logarithmic parameterization with smooth activation, where the variance is computed as

$$\sigma_\theta^2\left(x_i\right) = \ln\left(1 + \exp\left(g_\phi\left(x_i\right)\right)\right) \tag{8}$$

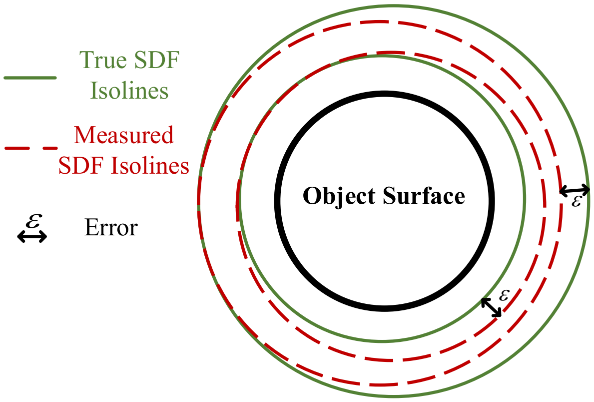

Fig. 3: SDF estimation is prone to inaccuracy, leading to measurement errors when used as supervisory labels.

where g_ϕ is a multi-layer perceptron that serves as the uncertainty prediction head. This formulation guarantees strictly positive variance while providing smooth gradients throughout the optimization process. The model is optimized using the negative log-likelihood of the heteroscedastic Gaussian model:

$$L_u = \frac{1}{2N}\sum_{i=1}^{N}\left[\frac{\left(s_i - \hat{s}_i\right)^2}{\sigma_\theta^2\left(x_i\right)} + \log\sigma_\theta^2\left(x_i\right)\right] \tag{9}$$

In (9), N is the number of training samples. This objective naturally balances prediction accuracy (first term) against uncertainty calibration (second term), preventing the network from artificially reducing loss by predicting unrealistically low uncertainties.

D. Odometry

Under error-free conditions, the SDF residual $\hat{s}$ derived from odometry measurements should be zero, which allows us to construct a least squares optimization problem. The optimal pose $\mathbf{T}^*$ is then determined by solving:

$$\mathbf{T}^* = \arg\min \sum_{a\in\mathcal{A}} \hat{s}_a^2 \tag{10}$$

where $\mathcal{A}$ denotes the set of all points. We solve (10) following the methodology presented in PIN-SLAM [15]. Our enhancement involves incorporating the predicted SDF uncertainty into the weight matrix of the Levenberg-Marquardt (LM) optimization framework. The experimental results in Section IV-B demonstrate that our uncertainty-weighted approach consistently outperforms PIN-SLAM in terms of localization precision across diverse environments.

E. Loss Function

In the context of signed distance function learning, binary cross-entropy loss (BCE) loss L_{bce} addresses the challenge that surface-proximate regions carry the most geometric significance while areas distant from surfaces contribute minimally to accurate reconstruction. We follow [3] for the definition and application of BCE loss. The output values are constrained to the range $[0, 1]$ through a sigmoid function $\Phi_s(s) = 1/\left(1 + e^{s/\sigma_t}\right)$ as

$$o_i = \Phi_s\left(s_i\right), \quad \hat{o}_i = \Phi_s\left(\hat{s}_i\right) \tag{11}$$

Therefore, the BCE loss for all N_i sampling points can be formulated as

$$L_{\text{bce}} = \frac{1}{N_i}\sum_{i=1}^{N_i} \hat{o}_i \log\left(o_i\right) + \left(1-\hat{o}_i\right)\log\left(1-o_i\right) \tag{12}$$

The eikonal loss L_{eik} enforces the constraint that the gradient norm of a function equals one, which is particularly crucial in neural implicit representations [30]. By ensuring that the learned neural network satisfies the eikonal property, this regularization term helps maintain geometric consistency and prevents the neural network from learning degenerate solution.

Overall, the total loss function L_{all} is formulated as

$$L_{\text{all}} = L_{\text{bce}} + \lambda_e L_{\text{eik}} + \lambda_u L_u \tag{13}$$

where λ_e and λ_u denote the respective hyperparameters.

For all experimental sequences, we set the downsampling parameter to 0.4, while the hyperparameters λ_e and λ_u are both set to 0.5. The MLP architecture consists of 2 layers with 64 neurons each. The uncertainty MLP includes an additional Softplus layer.

IV. EXPERIMENTS

A. Datasets

We conducted experiments using the following datasets. The MCD dataset [31] targets campus environments and employs a 128-beam Ouster LiDAR system, from which we select four sequences for evaluation. SubT-MRS [32] is a dataset specifically designed for underground environments, utilizing a 16-beam Velodyne LiDAR sensor. We evaluate our method on five sequences from this dataset. Additionally, our custom autonomous vehicle platform is equipped with a 32-beam Ouster LiDAR sensor. Data collection was performed in indoor environments, specifically within corridors and other enclosed spaces, as shown in Fig. 4. The datasets are labeled as Indoor01 and Indoor02. To evaluate mapping accuracy, we adopted the widely-used Newer College dataset [33], which serves as a standard benchmark for most mapping algorithms and provides centimeter-level ground truth mapping precision.

B. Localization Accuracy

We selected NeRF-LOAM [14], KISS-ICP [34], SLAMesh [35], PIN-SLAM [15], and CLID-SLAM [10] as baseline algorithms for comparative evaluation. KISS-ICP is a LiDAR odometry algorithm, and SLAMesh utilizes mesh information for odometry estimation. NeRF-LOAM, PIN-SLAM, and CLID-SLAM represent implicit LiDAR SLAM approaches. It should be noted that for this evaluation, we remove the IMU component from CLID-SLAM and employ a constant velocity model to predict the initial pose for each frame,

Fig. 4: The figure shows the unmanned vehicle equipped with a 32-line LiDAR sensor (left) and the indoor experimental environment containing narrow corridors and other indoor scenarios (right).

denoted as CLID. Additionally, NeRF-LOAM shows consistently poor performance on our platform across all tested scenarios. The results reported for NeRF-LOAM in the SubT-MRS dataset are referenced from [10]. In our experimental setup, all evaluated SLAM algorithms operate without loop closure modules to ensure consistent comparison conditions.

As shown in Table I, the root mean square error (RMSE) of localization is presented for all algorithms. The results in the table indicate that implicit SLAM approaches demonstrate superior accuracy compared to explicit methods. In outdoor scenarios such as MCD datasets, our proposed algorithm performs competitively with PIN-SLAM, showing comparable accuracy metrics. However, in indoor environments, as evaluated on the SubT-MRS and our dataset, our method exhibits a clear performance advantage. Fig. 5 presents the cumulative distribution function (CDF) analysis for our indoor scenarios. On the Indoor01 dataset, the 95% error bounds for our method, CLID, KISS-ICP, and PIN-SLAM are 0.409m, 0.973m, 5.199m, and 1.263m, respectively. Compared to the second-best performing algorithm, our method demonstrates an improvement of 57.97%. Similarly, on the Indoor02 dataset, the corresponding 95% error bounds are 0.327m, 0.437m, 1.166m, and 0.856m, respectively, with our method achieving an improvement of 25.17% over the second-best algorithm.

C. Mapping Accuracy

We evaluate our method using three sequences from the Newer College dataset, namely quad, math, and math0. Mapping performance was evaluated using the following metrics: Map Accuracy, Completion, Chamfer-L1, and F-score.

We conducted a mapping comparison with general SLAM methods (SLAMesh and PIN-SLAM) as well as mapping-focused approaches including Shine-Mapping [3] and UN3-Mapping [24]. The mapping results are presented in Table II, III, IV. SLAMesh represents an explicit mapping approach, and the results demonstrate that explicit methods generally underperform compared to implicit techniques. Our proposed algorithm achieves competitive advantages across all three sequences, consistently ranking highest in Completion, Chamfer-L1, and F-score metrics.

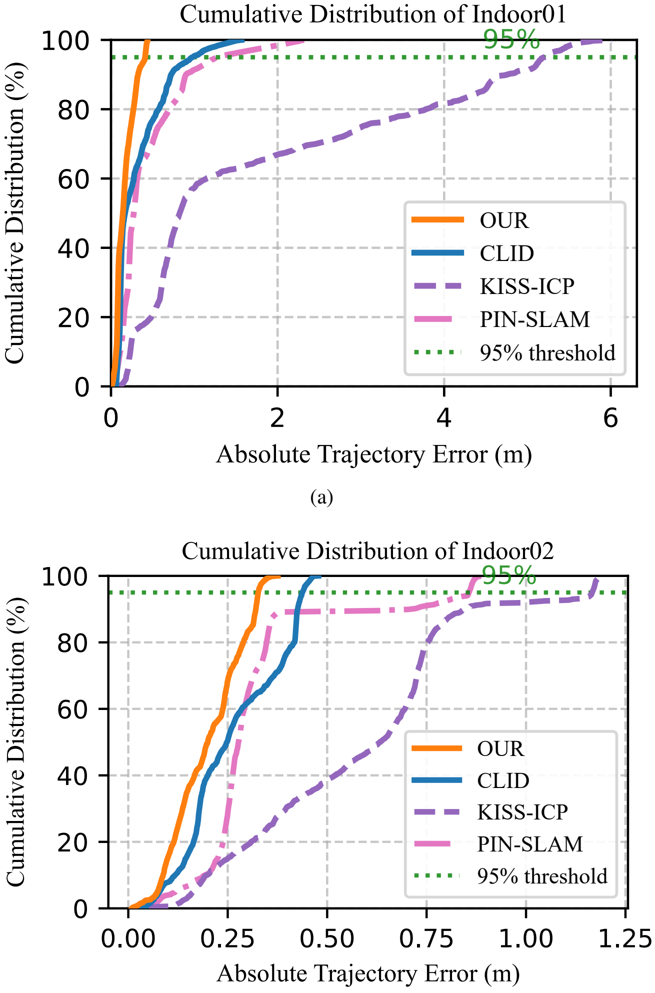

(a)

(b)

Fig. 5: Cumulative distribution function (CDF) analysis for (a) Indoor01 and (b) Indoor02. The green dashed line represents the 95% error threshold, demonstrating that our approach achieves better accuracy with the smallest errors compared to other baseline methods.

Fig. 6 presents a qualitative evaluation of our approach, showing the reconstructed mesh colored by surface normal vectors. The enlarged view on the right illustrates the reconstruction quality achieved in large-scale environments.

Our proposed algorithm is similar to UN3-Mapping but extends beyond basic mapping to include real-time localization capabilities. Fig. 7 illustrates detailed mapping results from both algorithms. Although UN3-Mapping produces relatively smoother reconstructions owing to its reliance on ground truth pose information, our method achieves better surface completeness with notably smaller holes and gaps, especially in the challenging scenarios shown in the bottom row of the

TABLE I: ACCURACY EVALUATION OF TRANSLATIONAL RMSE (M). **BOLD** INDICATES THE BEST RESULTS, AND UNDERLINE INDICATES THE SECOND-BEST RESULTS.

Algorithm	NTU02	NTU04	NTU08	NTU10	F_UGV1	F_UGV2	F_UGV3	U_UGV1	U_UGV2	Indoor01	Indoor02
NeRF-LOAM	×	×	×	×	×	×	×	0.58	×	×	×
KISS-ICP	0.33	1.88	2.67	2.16	1.28	1.13	18.73	0.41	1.54	2.19	0.45
SLAMesh	0.73	1.94	×	3.19	6.63	×	×	0.08	10.02	×	×
CLID	0.47	3.87	×	2.41	**0.38**	0.93	1.12	0.07	0.97	0.44	0.28
PIN-SLAM	**0.23**	**1.49**	2.34	**0.90**	0.59	0.33	1.34	0.07	×	0.61	0.37
OUR	**0.23**	1.71	**1.70**	1.08	0.42	**0.18**	**1.10**	**0.05**	**0.90**	**0.21**	**0.20**

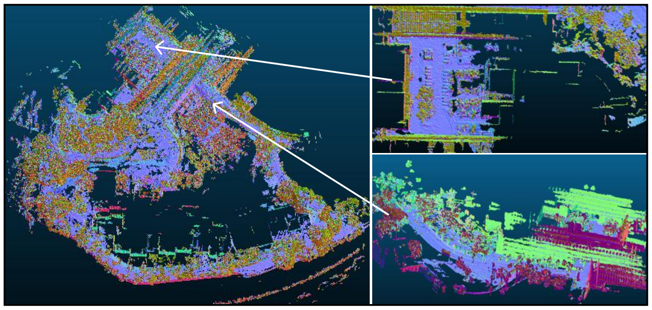

Fig. 6: The mapping results on the MCD datasets are visualized using normal vector-based coloring, with the enlarged view on the right illustrating the reconstruction quality achieved in large-scale environments.

Fig. 7.

TABLE II: QUAD DATASET MAPPING RESULTS

Algorithm	Map Acc (cm)↓	Comp (cm)↓	C_L1(cm)↓	F1-score(%)↑
SLAMesh	22.77	48.84	30.11	28.68
UN3-Mapping	18.18	15.53	13.69	81.32
Shine-Mapping	**13.54**	11.97	12.76	80.05
PIN-SLAM	15.02	11.37	13.19	77.53
OUR	14.62	**9.16**	**11.89**	**84.27**

TABLE III: MATH DATASET MAPPING RESULTS

Algorithm	Map Acc (cm)↓	Comp (cm)↓	C_L1(cm)↓	F1-score(%)↑
SLAMesh	21.76	39.32	25.05	48.16
UN3-Mapping	20.12	17.56	15.76	75.08
Shine-Mapping	**15.00**	13.94	14.46	74.46
PIN-SLAM	16.08	10.21	13.14	77.29
OUR	16.28	**9.32**	**12.80**	**81.16**

TABLE IV: MATH0 DATASET MAPPING RESULTS

Algorithm	Map Acc (cm)↓	Comp (cm)↓	C_L1(cm)↓	F1-score(%)↑
SLAMesh	21.61	46.47	28.64	40.32
UN3-Mapping	21.15	22.73	17.13	74.35
Shine-Mapping	14.16	14.12	14.14	77.10
PIN-SLAM	13.79	8.62	11.21	83.36
OUR	**13.19**	**7.80**	**10.49**	**87.16**

D. Ablation Study

To assess the individual contributions of normal vector-based sampling and confidence guidance, we conducted ablation studies denoted as w/o NS and w/o CG respectively, using the SubT-MRS underground dataset for validation. The experimental results are presented in Table V.

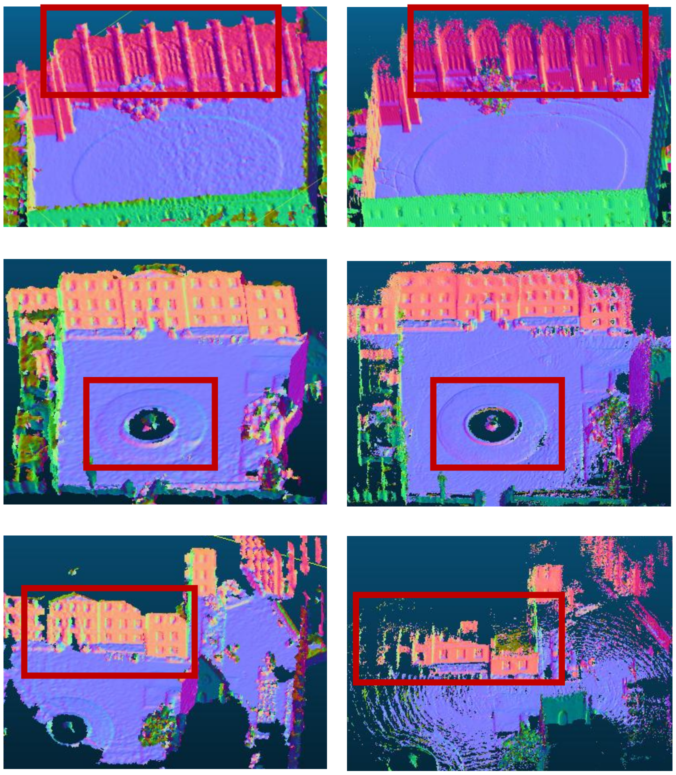

Fig. 7: The left column presents results from our proposed algorithm, while the right column shows results from UN3-Mapping. The figures display detailed mapping results for the quad, math, and math0 sequence from the Newer College dataset. Our algorithm exhibits significantly fewer mapping artifacts and void regions.

1) Confidence Guidance Module: Without the confidence evaluation module (i.e., using constant values instead of outputting uncertainty), the localization accuracy exhibits a slight degradation. As an uncertainty assessment mechanism, this module enables the selection of appropriate weights, thereby enhancing both localization and mapping accuracy. By adaptively adjusting the contribution of each sampling point based on its predicted uncertainty, it can effectively prioritize reliable measurements while reducing the influence of potentially erroneous data.

2) Sampling: Underground environments present unique challenges due to their complex geometric structures and limited surface diversity, making it crucial to intelligently

TABLE V: ABLATION EXPERIMENT RESULTS:INFLUENCE OF EACH MODULE ON POSITIONING ACCURACY (M)

Sequence	OUR (w/o NS)	OUR (w/o CG)	OUR
F_UGV1	0.68	0.43	**0.42**
F_UGV2	×	0.20	**0.18**
F_UGV3	1.18	1.20	**1.10**
U_UGV1	**0.05**	0.06	**0.05**
U_UGV2	1.52	1.12	**0.90**

The notation “w/o” denotes “without.”

prioritize sampling points that provide reliable geometric constraints. When the normal vector-based weight computation is disabled, our algorithm demonstrates a substantial degradation in localization accuracy, with the system even diverging completely in F_UGV2 sequence. This degradation arises because, without normal vector guidance, the system assigns equal importance to all sampling points, including those from uncertain or geometrically ambiguous regions, thereby propagating errors throughout the optimization process.

E. Parameter Analysis

Through our experiments, we observed that the parameter α in (2) has the most significant impact on system accuracy. This parameter controls the angle weighting computed from normal vectors, which directly influences the performance of SLAM systems. To validate this finding, we conducted experiments using the MCD dataset with varying parameter settings. As illustrated in Fig. 8, the localization RMSE varies considerably across different α values. The experimental results demonstrate that when α is set to 0.3, all four datasets achieve their minimum error values, confirming the critical role of proper angle weighting in achieving optimal accuracy.

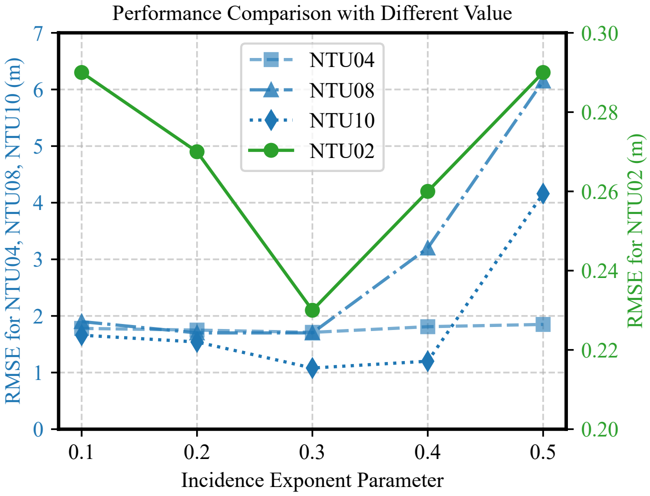

Fig. 8: Parameter sensitivity analysis for localization performance.

F. Time Cost

All experiments were conducted using an NVIDIA A5000 graphics processing unit equipped with 24 GB of video memory (VRAM). To evaluate the computational efficiency of individual system modules, we performed comprehensive timing analysis utilizing the Urban sequence from the SubT_MRS dataset. The results, presented in Table VI, indicate that although the mapping module constitutes the principal computational bottleneck, the overall system achieves an average per-frame processing time of less than 100ms, thus satisfying the real-time requirements of LiDAR sensors operating at 10Hz.

TABLE VI: COMPUTATIONAL TIME BREAKDOWN BY MODULE

Module	Time (ms)
Down sampling and motion compensation	1.46
Registration	29.84
Normal vector extraction	10.20
Sampling and map update	11.27
Mapping	40.67
Total	93.44

V. CONCLUSION AND OUTLOOK

In this work, we have addressed two critical limitations in implicit LiDAR SLAM systems: the lack of uncertainty quantification and the challenge of normal vector-driven sampling. Our proposed neural network-based approach successfully learns and estimates SDF uncertainty. And our approach computes ray weights based on surface normal information, leading to more accurate SDF training weight and improved mapping quality. Experimental validation on both public datasets and our custom platform demonstrates that our method achieves improvements in both localization accuracy and mapping robustness compared to other approaches. At the same time, our method maintains real-time computational performance.

Future work will explore the integration of semantic information to improve environmental structure understanding and object recognition capabilities within the implicit mapping framework. Furthermore, it is important to note that our current implementation requires moderate GPU computational resources, and optimization for deployment on resource-constrained platforms remains a priority for future development.

REFERENCES

[1] J. Zhang, S. Singh *et al.*, “Loam: Lidar odometry and mapping in real-time.” in *Robotics: Science and systems*, vol. 2, no. 9. Berkeley, CA, 2014, pp. 1–9.

[2] J. Paneque, J. R. M.-d. Dios, and A. Ollero, “Leveraging probabilistic meshes for robust lidar mapping,” *IEEE Transactions on Robotics*, vol. 41, pp. 4622–4642, 2025.

[3] X. Zhong, Y. Pan, J. Behley, and C. Stachniss, “Shine-mapping: Large-scale 3d mapping using sparse hierarchical implicit neural representations,” in *2023 IEEE International Conference on Robotics and Automation (ICRA)*, 2023, pp. 8371–8377.

[4] Y. Mao, X. Yu, Z. Zhang, K. Wang, Y. Wang, R. Xiong, and Y. Liao, "Ngel-slam: Neural implicit representation-based global consistent low-latency slam system," in *2024 IEEE International Conference on Robotics and Automation (ICRA)*, 2024, pp. 6952–6958.

[5] S. Chen, T. Chabal, I. Laptev, and C. Schmid, "Object goal navigation with recursive implicit maps," in *2023 IEEE/RSJ International Conference on Intelligent Robots and Systems (IROS)*, 2023, pp. 7089–7096.

[6] M. Yu, T. Lu, L. Xu, L. Jiang, Y. Xiangli, and B. Dai, "Gsdf: 3dgs meets sdf for improved neural rendering and reconstruction," *Advances in Neural Information Processing Systems*, vol. 37, pp. 129 507–129 530, 2024.

[7] J. Q. Yeo, A. B. Ng, K. Chen, P. Mohan, F. Guan, and S. See, "Pnp: A review framework towards efficient nerf study and research," in *Proceedings of the AAAI Symposium Series*, vol. 1, no. 1, 2023, pp. 35–39.

[8] X. Pan, Z. Lai, S. Song, and G. Huang, "Activenerf: Learning where to see with uncertainty estimation," in *European Conference on Computer Vision*. Springer, 2022, pp. 230–246.

[9] Y. Shen, L. Zhang, Q. Li, X. Zhao, Y. Wang, H. Lu, and X. Chen, "Ugna-vpr: A novel training paradigm for visual place recognition based on uncertainty-guided nerf augmentation," *IEEE Robotics and Automation Letters*, 2025.

[10] J. Jiang, X. Zhang, G. Sun, Y. Liu, X. Zhang, and Y. Zhuang, "Clid-slam: A coupled lidar-inertial neural implicit dense slam with region-specific sdf estimation," *IEEE Robotics and Automation Letters*, 2025.

[11] S. Song, J. Zhao, K. Huang, J. Lin, C. Ye, and T. Feng, "N3-mapping: Normal guided neural non-projective signed distance fields for large-scale 3d mapping," *IEEE Robotics and Automation Letters*, vol. 9, no. 6, pp. 5935–5942, 2024.

[12] C. Yuan, W. Xu, X. Liu, X. Hong, and F. Zhang, "Efficient and probabilistic adaptive voxel mapping for accurate online lidar odometry," *IEEE Robotics and Automation Letters*, vol. 7, no. 3, pp. 8518–8525, 2022.

[13] Z. Zhu, S. Peng, V. Larsson, W. Xu, H. Bao, Z. Cui, M. R. Oswald, and M. Pollefeys, "Nice-slam: Neural implicit scalable encoding for slam," in *2022 IEEE/CVF Conference on Computer Vision and Pattern Recognition (CVPR)*, 2022, pp. 12 776–12 786.

[14] J. Deng, Q. Wu, X. Chen, S. Xia, Z. Sun, G. Liu, W. Yu, and L. Pei, "Nerf-loam: Neural implicit representation for large-scale incremental lidar odometry and mapping," in *Proceedings of the IEEE/CVF International Conference on Computer Vision*, 2023, pp. 8218–8227.

[15] Y. Pan, X. Zhong, L. Wiesmann, T. Posewsky, J. Behley, and C. Stachniss, "Pin-slam: Lidar slam using a point-based implicit neural representation for achieving global map consistency," *IEEE Transactions on Robotics*, vol. 40, pp. 4045–4064, 2024.

[16] B. Fei, J. Xu, R. Zhang, Q. Zhou, W. Yang, and Y. He, "3d gaussian splatting as a new era: A survey," *IEEE Transactions on Visualization and Computer Graphics*, vol. 31, no. 8, pp. 4429–4449, 2025.

[17] K. Zhang, S. Xu, Y. Ding, X. Kong, and S. Wang, "Curl-slam: Continuous and compact lidar mapping," *IEEE Transactions on Robotics*, vol. 41, pp. 4538–4556, 2025.

[18] T. Tuna, J. Nubert, Y. Nava, S. Khattak, and M. Hutter, "X-icp: Localizability-aware lidar registration for robust localization in extreme environments," *IEEE Transactions on Robotics*, vol. 40, pp. 452–471, 2023.

[19] J. Zhang, M. Kaess, and S. Singh, "On degeneracy of optimization-based state estimation problems," in *2016 IEEE international conference on robotics and automation (ICRA)*. IEEE, 2016, pp. 809–816.

[20] H. Cho, S. Yeon, H. Choi, and N. Doh, "Detection and compensation of degeneracy cases for imu-kinect integrated continuous slam with plane features," *Sensors*, p. 935, Mar 2018.

[21] Y. Liu, J. Wang, and Y. Huang, "A localizability estimation method for mobile robots based on 3d point cloud feature," in *2021 IEEE International Conference on Real-time Computing and Robotics (RCAR)*. IEEE, 2021, pp. 1035–1041.

[22] S. Nobili, G. Tinchev, and M. Fallon, "Predicting alignment risk to prevent localization failure," in *2018 IEEE International Conference on Robotics and Automation (ICRA)*. IEEE, 2018, pp. 1003–1010.

[23] A. Kendall and Y. Gal, "What uncertainties do we need in bayesian deep learning for computer vision?" *Advances in neural information processing systems*, vol. 30, 2017.

[24] S. Song, J. Zhao, E. Veas, J. Lin, Q. Cao, C. Ye, and T. Feng, "Un3-mapping: Uncertainty-aware neural non-projective signed distance fields for 3d mapping," *IEEE Robotics and Automation Letters*, 2025.

[25] S. Wang, Y. Xie, C.-P. Chang, C. Millerdurai, A. Pagani, and D. Stricker, "Uni-slam: Uncertainty-aware neural implicit slam for real-time dense indoor scene reconstruction," in *2025 IEEE/CVF Winter Conference on Applications of Computer Vision (WACV)*. IEEE, 2025, pp. 2228–2239.

[26] K. Gui, Z. Chen, L. Chen, Z. Wang, M. Xu, and X. Pan, "Ucpin-slam: Lidar slam using implicit neural representations with uncertainty modeling," *IEEE Sensors Journal*, 2025.

[27] K. Huang, J. Zhao, Z. Zhu, C. Ye, and T. Feng, "Log-lio: A lidar-inertial odometry with efficient local geometric information estimation," *IEEE Robotics and Automation Letters*, vol. 9, no. 1, pp. 459–466, 2023.

[28] D. Chung and J. Kim, "Nv-liom: Lidar-inertial odometry and mapping using normal vectors towards robust slam in multifloor environments," *IEEE Robotics and Automation Letters*, 2024.

[29] C. Zhao, Y. Li, Y. Jian, J. Xu, L. Wang, Y. Ma, and X. Jin, "Ii-nvm: Enhancing map accuracy and consistency with normal vector-assisted mapping," *IEEE Robotics and Automation Letters*, 2025.

[30] J. Ortiz, A. Clegg, J. Dong, E. Sucar, D. Novotny, M. Zollhoefer, and M. Mukadam, "isdf: Real-time neural signed distance fields for robot perception," *arXiv preprint arXiv:2204.02296*, 2022.

[31] T.-M. Nguyen, S. Yuan, T. H. Nguyen, P. Yin, H. Cao, L. Xie, M. Wozniak, P. Jensfelt, M. Thiel, J. Ziegenbein *et al.*, "Mcd: Diverse large-scale multi-campus dataset for robot perception," in *Proceedings of the IEEE/CVF conference on computer vision and pattern recognition*, 2024, pp. 22 304–22 313.

[32] S. Zhao, Y. Gao, T. Wu, D. Singh, R. Jiang, H. Sun, M. Sarawata, Y. Qiu, W. Whittaker, I. Higgins *et al.*, "Subt-mrs dataset: Pushing slam towards all-weather environments," in *Proceedings of the IEEE/CVF Conference on Computer Vision and Pattern Recognition*, 2024, pp. 22 647–22 657.

[33] M. Ramezani, Y. Wang, M. Camurri, D. Wisth, M. Mattamala, and M. Fallon, "The newer college dataset: Handheld lidar, inertial and vision with ground truth," in *2020 IEEE/RSJ International Conference on Intelligent Robots and Systems (IROS)*, 2020, pp. 4353–4360.

[34] I. Vizzo, T. Guadagnino, B. Mersch, L. Wiesmann, J. Behley, and C. Stachniss, "Kiss-icp: In defense of point-to-point icp–simple, accurate, and robust registration if done the right way," *IEEE Robotics and Automation Letters*, vol. 8, no. 2, pp. 1029–1036, 2023.

[35] J. Ruan, B. Li, Y. Wang, and Y. Sun, "Slamesh: Real-time lidar simultaneous localization and meshing," in *2023 IEEE International Conference on Robotics and Automation (ICRA)*. IEEE, 2023, pp. 3546–3552.